

DIRECT NUMERICAL SIMULATION OF THE FLOW AROUND A WING SECTION USING HIGH-ORDER PARALLEL SPECTRAL METHODS

Ricardo Vinuesa

Linné FLOW Centre, KTH Mechanics
SE-100 44 Stockholm, Sweden
rvinuesa@mech.kth.se

Seyed M. Hosseini

Linné FLOW Centre, KTH Mechanics
SE-100 44 Stockholm, Sweden
hosse@mech.kth.se

Ardeshir Hanifi

Linné FLOW Centre, KTH Mech. and FOI
SE-100 44 Stockholm, Sweden
ardeshir@mech.kth.se

Dan S. Henningson

Linné FLOW Centre, KTH Mechanics
SE-100 44 Stockholm, Sweden
henning@mech.kth.se

Philipp Schlatter

Linné FLOW Centre, KTH Mechanics
SE-100 44 Stockholm, Sweden
pschlatt@mech.kth.se

ABSTRACT

The results of a DNS of the flow around a wing section represented by a NACA4412 profile, with $Re_c = 400,000$ and 5° angle of attack, are presented in this study. The high-order spectral element code Nek5000 is used for the computations. An initial RANS simulation is used to define the velocity boundary conditions, and to design the computational mesh. The agreement between spanwise- and time-averaged fields from the DNS and the RANS simulation is excellent. The mean flow and several components of the Reynolds stress tensor at $x/c = 0.4$ ($\beta = 0.53$) and 0.8 ($\beta = 4.54$) are compared with the ZPG boundary layer computed by Schlatter & Örlü (2010). In both cases, the friction Reynolds number is roughly matched (330 and 450), and as expected the Re_θ values from the wing (720 and 1,800) are larger than the ones from the ZPG case (612 and 1,007). The APG leads to a steeper log law, a more prominent wake region and a larger U_e^+ . The tangential turbulence intensity exhibits a stronger inner peak, and starts to develop an outer peak. We also show that the impact on the spanwise component is significant, and also on the wall-normal intensity and the Reynolds shear stress for stronger pressure gradients, especially in the outer region.

MOTIVATING PROBLEM

A clear evolutionary path can be observed looking back at the aircrafts from early days and comparing them to the state of the art modern civil aircrafts. This by large is owed to deeper understanding of the different flow phenomena taking place in such configurations, i.e., laminar-turbulent transition, wall-bounded turbulence subjected to pressure gradients and wall curvature, flow separation, turbulent wake flow, etc. Despite the conspicuous advances in aircraft design, major challenges still remain, mainly re-

garding our understanding of the complex flow phenomena and new design strategies targeted at efficiently exploiting the interacting features on an airplane. Traditionally such procedures relied heavily on experimental findings and rules of thumb derived from experience. Recent advances in supercomputers and massive parallelization have resulted in a vast number of parameters impacting the design of the aircraft. These parameters can be optimized via computational resources with the aim of reducing development cost and enhancing efficiency.

A recent report by NASA (Slotnick *et al.*, 2014) discusses a number of findings and recommendations regarding the present and future role of CFD (computational fluid dynamics) in aircraft design. The main revelations point out the necessity of accurate predictions of turbulent flows with significantly separated regions, more robust, fast and reliable mesh generation tools and the development of multidisciplinary simulations (such as fluid-structure interaction, conjugate heat transfer or aeroacoustics) for both analysis and optimization procedures. Industrial computations of aircraft components are mainly based on Reynolds-Averaged Navier-Stokes (RANS) simulations, where turbulence is modeled relying on empirical arguments. This approach only allows proper characterization of simple flow features (such as lift and drag) after proper tuning based on equivalent wind tunnel tests. Other numerical approaches, such as direct numerical simulation (DNS, where all the turbulent scales are resolved) and large eddy-simulation (LES, which relies on modeling only the smallest, more homogeneous scales in the flow), allow a much better characterization of the complex flow features in an aircraft. This significantly increases the possibilities for optimization. According to researchers from The Boeing Company, a reduction of only 2% in skin friction leads to 1% reduction in total drag. Keeping in mind that around 700 billion gallons of

oil were used in 2006 for transportation world-wide (as reported by the US Energy Information Administration, EIA), there is a huge potential of improvement in energy savings and fuel consumption.

DNS OF THE FLOW AROUND A NACA4412 WING SECTION

In this study we perform a fully-resolved DNS of the flow around a wing section, at a Reynolds number comparable with the ones characteristic of academic wind tunnel experiments. Available numerical studies of this configuration are limited to low Reynolds numbers up to around $Re_c \simeq 100,000$ (where Re_c is the Reynolds number based on freestream velocity U_∞ and wing chord length c). These studies include low-order DNSs (Rodríguez *et al.*, 2013) and LESs (Alferez *et al.*, 2013), as well as some high-order DNSs (Shan *et al.*, 2005), and are all performed on the symmetric NACA0012 profile. High-order numerical methods are required for accurate simulations of turbulent flows due to the significant scale disparity of the flow structures, both in time and space. Here we present the first results of a DNS of the flow around a NACA4412 wing profile at $Re_c = 400,000$ with 5° angle of attack. Note that whereas the emphasis in other cases was on high angles of attack and stalled airfoils, here we consider a small angle of attack so that the flow will be attached throughout most of the suction side of the wing. The relevance of this flow case lies in the significantly higher Reynolds number compared with other studies, and in the additional flow complexity introduced by the cambered airfoil.

Numerical code

The numerical code chosen for this project is Nek5000, developed by Fischer *et al.* (2008) at the Argonne National Laboratory, and based on the spectral element method (SEM), originally proposed by Patera (1984). This discretization allows to combine the geometrical flexibility of finite elements with the accuracy of spectral methods. The spatial discretization is done by means of the Galerkin approximation, following the $\mathbb{P}_N - \mathbb{P}_{N-2}$ formulation. The solution is expanded within a spectral element in terms of three Legendre polynomials of order N (of order $N - 2$ in the case of the pressure), at the Gauss-Lobatto-Legendre (GLL) quadrature points. The nonlinear terms are treated explicitly by third-order extrapolation (EXT3), whereas the viscous terms are treated implicitly by a third-order backward differentiation scheme (BDF3). Nek5000 is written in Fortran 77 and C, and parallel I/O is supported both through MPI I/O and a custom parallel I/O implementation. Over 190 users worldwide employ Nek5000 for their research and it has been acknowledged in more than 200 journal articles. In our research group, results obtained with Nek5000 have been reported in more than 20 publications in leading fluid mechanics journals over the last 5 years. The simulations were carried out on the Cray XC40 system ‘Beskow’ at the PDC Center from KTH in Stockholm (Sweden), running on 16,384 cores, and the message-passing interface (MPI) was employed for parallelization.

Numerical setup

The flow was initially characterized by performing a detailed RANS simulation based on the explicit algebraic Reynolds stress model (EARSM) by Wallin & Johansson

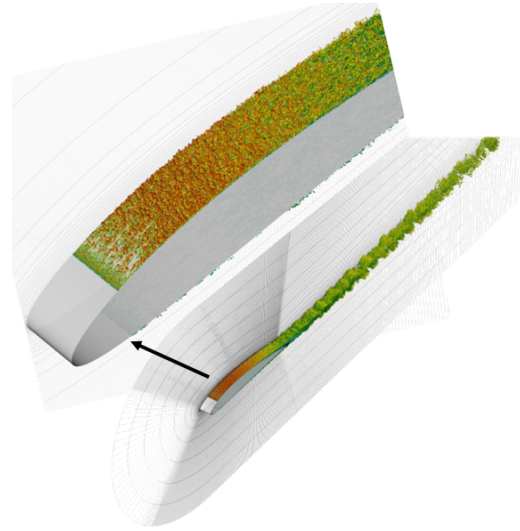


Figure 1. Instantaneous visualization of the DNS results showing coherent vortices identified by means of the λ_2 criterion (Jeong & Hussain, 1995). The spectral element mesh is also shown, but not the individual grid points within elements.

(2000). A very large circular domain of radius $200c$ was considered in the RANS simulation in order to reproduce free flight conditions. Since the focus of our study is on characterizing the flow around the wing section, we used a smaller computational domain for the DNS. In particular, we considered a C-mesh of radius c centered at the leading edge of the airfoil, with total domain lengths of $6.2c$ in the horizontal (x), $2c$ in the vertical (y) and $0.1c$ in the spanwise (z) directions. The resulting spectral element mesh (without the GLL points) and the computational domain are shown in Figure 1. The solution from the RANS simulation was used as boundary condition on all the domain boundaries except the outflow (where the natural stress-free condition is enforced) and in the spanwise direction, where periodicity is assumed. Although in other external flows where the stress-free condition was considered at the outflow we had to use a fringe upstream of the outlet in order to ensure numerical stability (such as in the flow around a wall-mounted square cylinder computed by Vinuesa *et al.* (2015)), in this case the fringe was not necessary. Also note that both in the RANS and the DNS the wing was placed forming 0° with the horizontal direction, and the 5° angle of attack was introduced through the freestream velocity vectors.

Mesh generation is one of the key factors of the present project, where the computational grid must meet the requirements for a fully-resolved DNS by allowing sufficient geometrical flexibility. The mesh is structured, and is designed to meet the following criteria around the wing section: $\Delta x^+ < 10$, $\Delta y_w^+ < 0.2$ (at the wing surface) and $\Delta z^+ < 5$. Note that here ‘+’ denotes scaling with the viscous length $\ell^* = \nu/u_\tau$ (where ν is the fluid kinematic viscosity and $u_\tau = \sqrt{\tau_w/\rho}$ is the friction velocity), or inner scaling. Since the wall shear stress τ_w is not constant over the wing surface, we considered the RANS results to design the mesh according to the following guidelines:

- (i) Between $x/c = 0.1$ and 0.6 , the u_τ from the RANS was used to compute Δx , both on suction and pressure sides.

- (ii) For $x/c > 0.6$, the u_τ from the RANS on the pressure side was used to design the mesh in x , both on the suction and pressure sides. The strong adverse pressure gradient (APG) on the suction side in this region leads to a progressively smaller value of u_τ , which in principle would yield a coarser mesh. However, we considered that at least the resolution of the pressure side should be used in this region of the upper surface.
- (iii) For $x/c < 0.1$, the respective values of u_τ at $x/c = 0.1$ on suction and pressure sides were used to design the mesh in x .
- (iv) The spectral element mesh is uniform in z , and the value of u_τ at $x/c = 0.2$ on the suction side was used to define the constant spanwise width of the spectral elements.
- (v) The mesh around the wing is orthogonal, and the Δy_w value was computed based on the value of u_τ close to the trailing edge on the pressure side.

Typical mesh requirements for DNS have been developed for canonical flow cases, where it is easy to define the wall shear stress and the parallel/orthogonal directions. However, they do not necessarily apply to the mesh around a wing section, especially farther from the wall, and therefore we developed additional criteria to ensure that the mesh requirements were met everywhere in the domain. To this end, we used distributions of the Kolmogorov scale η obtained from the RANS to optimize the mesh. Note that the Kolmogorov scale is computed as $\eta = (\nu^3/\varepsilon)$, where ε is the local isotropic dissipation. State-of-the-art high-Reynolds number DNSs (Schlatter & Örlü, 2010; Sillero *et al.*, 2013) typically follow $\Delta y(y) \sim 4 - 8\eta(y)$, which together with the previous restrictions in Δx and Δz provide sufficient mesh resolution for a fully resolved DNS. In our case, our mesh was designed ensuring that $(\Delta x \cdot \Delta y \cdot \Delta z)^{1/3} \sim 4 - 5\eta$ everywhere in the domain, which makes sure that the mesh is fine enough to capture the smallest turbulent scales. This can be observed in Figure 1, where the coherent vortices identified by means of the λ_2 criterion (Jeong & Hussain, 1995) are perfectly represented by the computational mesh. In this figure it can also be observed that the flow is tripped at 10% chord distance from the leading edge on both pressure and suction sides, following the approach by Schlatter & Örlü (2012). The tripping consists of wall-normal forcing producing strong, instationary streaks which eventually break down leading to a transition process similar to the one produced by the devices used in wind tunnel experiments. The smoothness of the hairpin vortices, characteristic of transitional flows, also shows that the mesh is appropriate to capture the most relevant flow features.

The spectral element method ensures C^0 continuity across element boundaries, which means that in principle fluxes of the various quantities do not necessarily have to be continuous between elements. However, our previous results show that if the polynomial order is high enough it is possible to obtain such continuity. For instance, in Vinuesa *et al.* (2014a) we show that using polynomial order $N = 11$ the instantaneous streamwise vorticity of a turbulent duct is smooth and continuous between spectral elements. Therefore, we decided to design our mesh meeting the previous requirements with $N = 11$, which led to a total of around 1.85 million spectral elements and 3.2 billion grid points. We started the simulation with a coarser resolution (same spectral element mesh but lower polynomial order) and used the solution from the RANS as initial

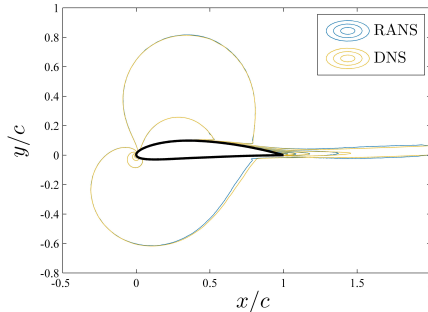


Figure 2. Comparison of the time- and spanwise-averaged horizontal velocity from the DNS and the RANS solution.

condition. We ran for several flow-over times (where U_∞ and c are used to nondimensionalize the time) with $N = 5$ and then with $N = 7$ until the flow settled, reaching a fully-developed turbulent state. At this point (and after running for around 10 flow-over times), we increased N to 11, and started the production runs. We collect turbulence statistics for around 10 additional flow-over times, which are approximately 12 eddy turnover times (where u_τ and the boundary layer thickness δ are used to scale the time). This choice is based on the recent high- Re channel flow DNSs by Lozano-Durán & Jiménez (2014), where they showed that turbulence statistics can be considered converged in our Reynolds number range when averaged for around 12 eddy turnover times. The values of δ and u_τ used to define the time scale were obtained at $x/c \simeq 0.8$, which is upstream of the region where instantaneous separation occurs. Note that although instantaneously detached flow can be observed for $x/c > 0.9$, inspection of the averaged flow shows attached boundary layers up to the trailing edge. The flow case presented here requires around 3 million CPU core hours per flow-over time on 16,384 cores on a CrayXC40, and therefore the approximate cost of the production runs is 30 million core hours. The results presented in this study are obtained after collecting statistics for around 4 flow-over times, which in principle is not sufficient to obtain fully converged turbulence budgets, but our mean flow and r.m.s. (root-mean-squared) velocities already exhibit convergence. Figure 2 shows a comparison of the horizontal velocity from the RANS and the one obtained from time- and spanwise-averaged fields from the DNS. The excellent agreement is quite remarkable, and also highlights the quality of the setup used in the present study.

RESULTS

In order to properly evaluate the impact of pressure gradient and wall curvature on the turbulent boundary layer developing over the suction side of the wing, we compute a complete set of turbulence statistics, including full budgets of all the components of the Reynolds stress tensor. To this end, we calculate spanwise- and time-averages of a total of 60 quantities during the simulation, and store them in binary files containing two-dimensional fields. These fields include instantaneous double and triple velocity products, pressure-strain products, etc., and are represented in the spectral element mesh. At the end of the simulation these fields are interpolated spectrally on a mesh consisting of a number of profiles normal to the wing surface, and rear-

ranged to form the various budgets. The derivatives are also evaluated spectrally on the SEM mesh, and interpolated afterwards on the grid normal to the wing surface. Note that tensor rotation was used to express all the quantities in the tangential (t) and normal (n) directions to the wing surface, where most tensors were of second order. The only third order tensor is the one corresponding to the triple velocity products, which requires the multiplication of three rotation matrices based on the local angle defined by the geometry of the wing.

Figure 3 shows the friction Reynolds number $Re_\tau = \delta u_\tau / \nu$ and the Reynolds number based on momentum thickness $Re_\theta = U_e \theta / \nu$ as a function of the horizontal position on the suction side of the wing. The velocity profiles used to evaluate these quantities are projected on t and n directions, at a total of 80 locations throughout the suction side. Note that here we use the local edge velocity U_e (in the direction tangential to the wing surface), defined as the location where $\partial U_t^+ / \partial y_n^+ \simeq 0$, to define Re_θ . It is interesting to observe how Re_θ grows along the suction side of the wing, where the rate of growth of the momentum thickness is greatly influenced by the APG. On the other hand, Re_τ increases (with small regions of local decrease) up to $x/c \simeq 0.9$, the point after which the trend is decreasing. This interesting behavior is due to the fact that Re_τ mixes the increasing trend of δ with the decreasing u_τ . After $x/c \simeq 0.9$ the APG is so strong that the boundary layer is close to detachment, with the corresponding significant decrease in wall shear stress. As stated above, the flow instantaneously detaches in this region, but spanwise- and time-averaged profiles are attached up to the trailing edge. At $x/c \simeq 0.9$ the following Reynolds numbers are obtained: $Re_\tau \simeq 467$ and $Re_\theta \simeq 2,300$. The closest zero pressure gradient (ZPG) boundary layer simulated with DNS by Schlatter & Örlü (2010) has $Re_\tau \simeq 490$ and $Re_\theta \simeq 1,420$. Note the effect of the APG: for roughly the same friction Reynolds number the momentum thickness of the ZPG is 40% smaller than that of the boundary layer developing over the wing. This highlights the fact that the APG strongly reduces wall shear by lifting up the profile, and therefore the APG boundary layer carries more momentum overcoming basically the same friction. This is also observed in the value of the shape factor $H = \delta^* / \theta$ (where δ^* is the displacement thickness), which is 1.43 in the ZPG case by Schlatter & Örlü (2010) and 2.03 at this particular location of the wing. In the following section we will discuss that the higher value of H is in agreement with canonical APG boundary layers, which are much thicker than their ZPG counterpart.

Figure 4 shows the averaged fields of horizontal velocity (not rotated for simplicity) and pressure around the wing. Note that the reference pressure is obtained in our simulation as the average pressure between $x/c = 0.3$ and 0.5 , both on suction and pressure sides. These figures clearly show the location of the stagnation point (characterized by very high positive pressure), defined by the 5° angle of attack, and how the flow accelerates on the suction side due to the effect of the favorable pressure gradient (FPG) around the leading edge of the wing. A region of strong suction is observed up to around $x/c \simeq 0.6$, where the boundary layer remains relatively thin. After this point the significant APG leads to a progressively thicker boundary layer, as can be observed close to the trailing edge in connection with Figure 3. Note that although negative horizontal velocity values are observed in Figure 4 (left), the velocities become positive when projected on the t direction, thus yielding no

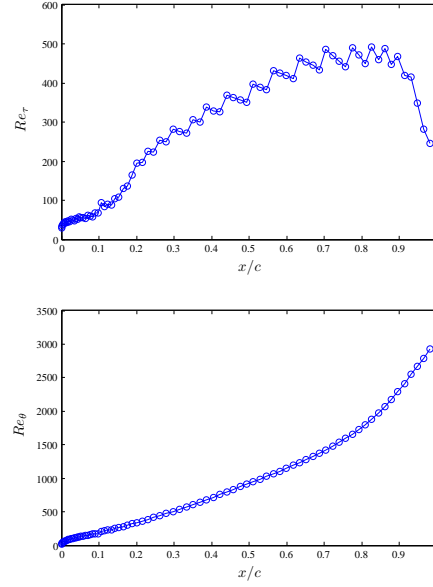


Figure 3. (Top) Friction Reynolds number and (bottom) Reynolds number based on momentum thickness, obtained from spanwise- and time-averaged velocity profiles. Note that the shape of the Re_τ curve is due to the fact that this quantity mixes the increasing trend of δ with the decreasing u_τ .

detachment in the mean, although close to $x/c \simeq 0.95$ the flow is very close to separation.

The inner-scaled mean flow is shown in Figure 5 at $x/c = 0.4$ and 0.8 , and compared with ZPG boundary layers from Schlatter & Örlü (2010). We selected the ZPG profiles that roughly matched Re_τ , following the approach by Monty *et al.* (2011) to analyze pressure gradient effects. The wing profile at $x/c = 0.4$ has $Re_\tau = 330$ and $Re_\theta = 720$, whereas the corresponding ZPG profile has $Re_\tau = 340$ and $Re_\theta = 612$. In order to characterize the pressure gradient at that particular location, we consider the Rotta-Clauser pressure gradient parameter $\beta = -\Delta / u_\tau dU_e / dx_t$, where $\Delta = U_e^+ \delta^*$ is the Rotta-Clauser length scale, and dU_e / dx_t is the derivative of the (projected) edge velocity with respect to the tangential direction t . At $x/c = 0.4$ the value of β is 0.53, which is associated with a moderate adverse pressure gradient. Localized pressure gradients of similar magnitude were studied experimentally and computationally by Vinuesa *et al.* (2014b) over a higher Reynolds number range up to $Re_\theta \simeq 35,000$. The effect of this moderate pressure gradient on the flow is noticeable especially in the outer part of the boundary layer, where a more prominent wake is observed, together with a higher value of inner-scaled edge velocity. The shape factor is also higher in the wing case (1.59) than in the ZPG (1.52). Although the Reynolds number is too low to observe a distinguishable logarithmic region, the composite profile by Nagib & Chahuan (2008) can be used to determine the values of the von Kármán coefficient κ , the log law intercept B and the wake parameter Π . In the ZPG boundary layer these parameter take the values $\kappa = 0.41$, $B = 5.1$ and $\Pi = 0.31$, whereas in the wing profile $\kappa = 0.38$, $B = 4.2$ and $\Pi = 0.57$. Although these values do not correspond to the asymptotic ones due to the low Reynolds number, the typical effects of the APG

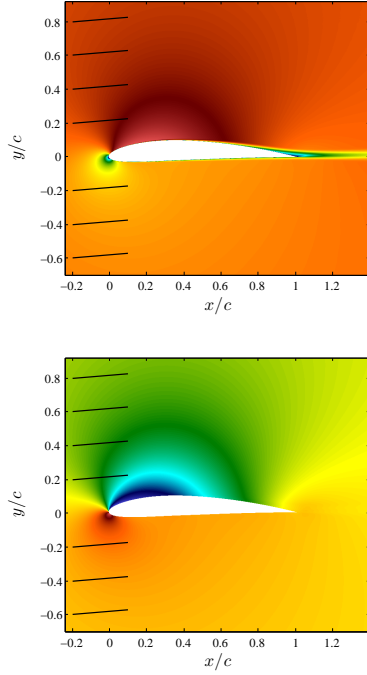


Figure 4. (Top) Spanwise- and time-averaged horizontal velocity and (bottom) pressure around the wing (reference pressure is obtained as the average pressure between $x/c = 0.3$ and 0.5 , both on suction and pressure sides). On the top panel the values range from -0.16 (dark blue) to 1.46 (dark red), whereas on the bottom one the range is from -0.51 to 0.67 . Black lines indicate the direction of the freestream in both cases.

on a boundary layer are observed: the logarithmic region becomes steeper, which leads to lower values of κ and B , and the wake becomes more prominent, with larger deviation from the log law. The wing profile at $x/c = 0.8$ has $Re_\tau = 450$ and $Re_\theta = 1,800$, and in this case the ZPG values are $Re_\tau = 455$ and $Re_\theta = 1,007$. At this location the APG is quite strong ($\beta = 4.54$), similar in magnitude to the strongest analyzed by Monty *et al.* (2011) on boundary layers with Re_θ up to 18,500. The stronger pressure gradient shows a significant effect in the outer flow, where the U_e^+ value is around 40% larger, but is also noticeable in the incipient logarithmic region and all the way down to the buffer layer. This is a consequence of the interaction between the APG and the largest structures of the flow, which leave their footprint at the wall. In this case the shape factor from the wing profile is 1.77, and the one from the ZPG boundary layer is 1.45. The effects of the APG on the log region discussed above are more prominent in this case, where the parameters from the wing profile are $\kappa = 0.31$, $B = 1.57$ and $\Pi = 1.42$, whereas the ones from the ZPG case are $\kappa = 0.40$, $B = 4.78$ and $\Pi = 0.36$.

Additional insight on the effect of APGs on the boundary layer developing over the wing can be gained by analyzing the components of the Reynolds stress tensor shown in Figure 6. Note that here we show the components projected on the t and n directions, and therefore the spanwise turbulence intensity $\overline{w^2}^+$ remains unchanged, and the Reynolds shear stress is defined as $\overline{u_t u_n}^+$. It can be observed how

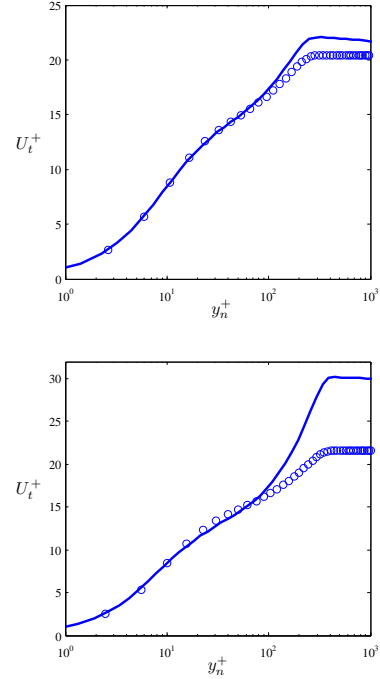


Figure 5. Inner-scaled mean velocity profiles from the present simulation (solid lines) and ZPG boundary layers by Schlatter & Örlü (2010) (circles, only every fourth point shown for clarity). Wing profiles at (top) $x/c = 0.4$ and (bottom) $x/c = 0.8$.

at $x/c = 0.4$ the pressure gradient has a large impact on the tangential turbulence intensity $\overline{u_t^2}^+$: the inner peak is increased, and the effect on the outer region is quite noticeable, as also observed by Monty *et al.* (2011). This is associated with the largest and most energetic scales in the flow interacting with the APG, as is also noticeable from the largest values of $\overline{w^2}^+$ in the outer region. It is also interesting to note that the effect on the wall-normal turbulence intensity $\overline{u_n^2}^+$ and the Reynolds shear stress is less noticeable than in the other two stresses. On the other hand, the APG greatly affects all the Reynolds stresses at $x/c = 0.8$, where the pressure gradient is strong. The tangential turbulence intensity exhibits a larger inner peak, and most interestingly starts to develop a prominent outer peak, as also observed by Monty *et al.* (2011). The APG leads to more energetic structures far from the wall, and since this outer peak is also observed in high Reynolds number boundary layers with no pressure gradient (Vallikivi, 2014), it will be interesting to further analyze the connections between high Reynolds number effects and pressure gradients in terms of modifications of the large-scale structures in the flow. This strong APG also leads to significantly larger values of the other components of the Reynolds stress tensor, especially in the outer region, including the wall-normal turbulence intensity and the Reynolds shear stress.

SUMMARY AND CONCLUSIONS

In the present study we perform a DNS of the flow around a wing section represented by a NACA4412 profile, with $Re_c = 400,000$ and 5° angle of attack. The high-

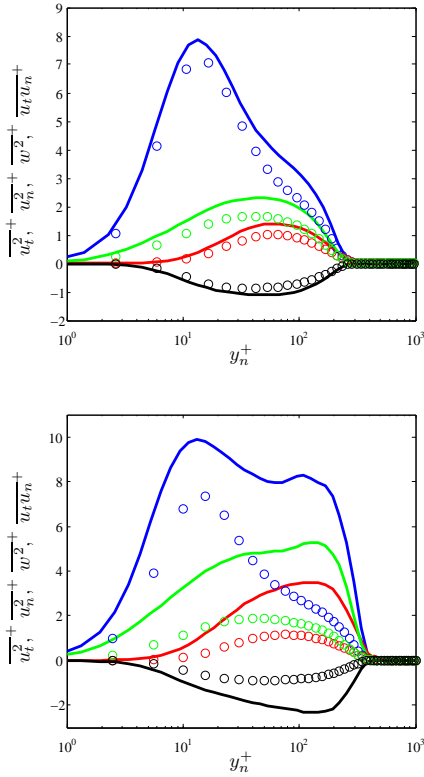


Figure 6. Selected inner-scaled components of the Reynolds stress tensor. Legend as in Figure 5.

order spectral element code Nek5000 is used for the computations, which are carried out with 16,384 cores on the Cray XC40 system “Beskow” in KTH, Stockholm. An initial RANS simulation is used to define the velocity boundary conditions, at to design the computational mesh which is carefully optimized in terms of viscous and Kolmogorov scale distributions. With the setup presented here we are able to simulate even the smallest turbulent structures, and the agreement between spanwise- and time-averaged fields with the RANS simulation is excellent.

Turbulence statistics are computed at a total of 80 locations over the suction side of the wing, and expressed in local tangential and normal directions. The Reynolds numbers at $x/c = 0.9$ are $Re_\tau \simeq 467$ and $Re_\theta \simeq 2,300$. The mean flow and several components of the Reynolds stress tensor at $x/c = 0.4$ and 0.8 are compared with the ZPG boundary layer computed by Schlatter & Örlü (2010). In both cases, the friction Reynolds number is roughly matched (330 and 450), and as expected the Re_θ values from the wing (720 and 1,800) are larger than the ones from the ZPG case (612 and 1,007). This is due to the fact that an APG boundary layer is able to carry more momentum than a ZPG, overcoming the same friction. The APG is moderate at $x/c = 0.4$ ($\beta = 0.53$) and strong at $x/c = 0.8$ ($\beta = 4.54$). Its effect on the mean flow is consistent with previous observations (Vinuesa *et al.*, 2014b; Monty *et al.*, 2011), namely a steeper log law, a more prominent wake region and a larger U_e^+ . The effect of an APG on the tangential turbulence intensity was studied by Monty *et al.* (2011), and our findings are consistent with previous analyses: the inner peak increases, and an outer peak starts to develop with progres-

sively stronger APGs. Here we also show that the impact on w^{2+} is significant, and also on u_n^{2+} and $\overline{u_t u_n^+}$ for stronger pressure gradients, especially in the outer region.

REFERENCES

- Alferez, N., Mary, I. & Lamballais, E. 2013 Study of stall development around an airfoil by means of high fidelity large eddy simulation. *Flow Turb. Comb.* **91**, 623–641.
- Fischer, P. F., Lottes, J. W. & Kerkemeier, S. G. 2008 Nek5000: Open source spectral element CFD solver. Available at: <http://nek5000.mcs.anl.gov>.
- Jeong, J. & Hussain, F. 1995 On the identification of a vortex. *J. Fluid Mech.* **285**, 69–94.
- Lozano-Durán, A. & Jiménez, J. 2014 Effect of the computational domain on direct simulations of turbulent channels up to $Re_\tau = 4200$. *Phys. Fluids* **26**, 011702.
- Monty, J. P., Harun, Z. & Marusic, I. 2011 A parametric study of adverse pressure gradient turbulent boundary layers. *Int. J. Heat Fluid Flow* **32**, 575–585.
- Nagib, H. M. & Chahuan, K. A. 2008 Variations of von Kármán coefficient in canonical flows. *Phys. Fluids* **20**, 101518.
- Patera, A. T. 1984 A spectral element method for fluid dynamics: laminar flow in a channel expansion. *J. Comput. Phys.* **54**, 468–488.
- Rodríguez, I., Lehmkuhl, O., Borrell, R. & Oliva, A. 2013 Direct numerical simulation of a NACA0012 in full stall. *Int. J. Heat Fluid Flow* **43**, 194–203.
- Schlatter, P. & Örlü, R. 2010 Assessment of direct numerical simulation data of turbulent boundary layers. *J. Fluid Mech.* **659**, 116–126.
- Schlatter, P. & Örlü, R. 2012 Turbulent boundary layers at moderate Reynolds numbers. Inflow length and tripping effects. *J. Fluid Mech.* **710**, 5–34.
- Shan, H., Jiang, L. & Liu, C. 2005 Direct numerical simulation of flow separation around a NACA0012 airfoil. *Comput. Fluids* **34**, 1096–1114.
- Sillero, J. A., Jiménez, J. & Moser, R. D. 2013 One-point statistics for turbulent wall-bounded flows at Reynolds numbers up to $\delta^+ \simeq 2000$. *Phys. Fluids* **25**, 105102.
- Slotnick, J., Khodadoust, A., Alonso, J., Darmofal, D., Gropp, W., Lurie, E. & Mavriplis, D. 2014 CFD Vision 2030 Study: A Path to Revolutionary Computational Aeronautics. Tech. Rep. NASA/CR2014-218178.
- Vallikivi, M. 2014 Wall-bounded turbulence at high Reynolds numbers. PhD thesis, Princeton University.
- Vinuesa, R., Noorani, A., Lozano-Durán, A., El Khoury, G. K., Schlatter, P., Fischer, P. F. & Nagib, H. M. 2014a Aspect ratio effects in turbulent duct flows studied through direct numerical simulation. *J. Turbul.* **15**, 677–706.
- Vinuesa, R., Rozier, P. H., Schlatter, P. & Nagib, H. M. 2014b Experiments and computations of localized pressure gradients with different history effects. *AIAA J.* **52**, 368–384.
- Vinuesa, R., Schlatter, P., Malm, J., Mavriplis, C. & Henningson, D. S. 2015 Direct numerical simulation of the flow around a wall-mounted square cylinder under various inflow conditions. *J. Turbul.* **16**, 555–587.
- Wallin, S. & Johansson, A. V. 2000 An explicit algebraic Reynolds stress model for incompressible and compressible turbulent flows. *J. Fluid Mech.* **403**, 89–132.